Empirical Dust Attenuation Models: Taking Hydrodynamical Simulatons with a Grain of Dust

ChangHoon Hahn,[1, 2, 3, *] Tjitske K. Starkenburg,[4] and IQ Collaboratory

[1]*Department of Astrophysical Sciences, Princeton University, Peyton Hall, Princeton NJ 08544, USA*
[2]*Lawrence Berkeley National Laboratory, 1 Cyclotron Rd, Berkeley CA 94720, USA*
[3]*Berkeley Center for Cosmological Physics, University of California, Berkeley CA 94720, USA*
[4]*Center for Interdisciplinary Exploration and Research in Astrophysics (CIERA) and //Department of Physics and Astronomy, 1800 Sherman Ave, Evanston IL 60201, USA*

(Dated: `DRAFT -- 1c52723 -- 2020-10-27 -- NOT READY FOR DISTRIBUTION`)

ABSTRACT

We present the Empirical Dust Attenuation (EDA) models, an empirical framework for applying dust attenuation to simulated galaxy populations. The EDAuses a parameterization of the attenuation curve based on observational constraints and a statistical prescription for sampling the curves that includes correlations with galaxy properties. We apply the EDAto three state-of-the-art hydrodynamical simulations, SIMBA, Illustris TNG, and EAGLE. Then we forward model the spectral energy distributions and optical and UV color-magnitude relations, $(G-R) - M_r$ nd $(FUV-NUV) - M_r$, for the simulated galaxies and compare them to the central galaxies in SDSS using Approximate Bayesian Computation. For all three simulations, we are able to reproduce SDSS observations with the EDA. We find that SIMBA overpredicts low mass starburst galaxies and requires extreme EDAthat reverses the established relation between galaxy color and SFR. Since we can reproduce observations for disparate galaxy populations by varying dust attenuation, we demonstrate that dust is highly degenerate with subgrid physics in galaxy formation models. In addition to the observed color-magnitude relations, the EDAalso reproduces the observed attenuation–slope relation better than radiative transfer models. The predicted attenuation curves for star-forming galaxies are in good agreement with the literature. Furthermore, using the EDAwe find correlations between dust attenuation and galaxy properties: more massive galaxies have higher dust attenuation; galaxies with lower SFR have higher dust attenuation **TKS:** this seems weird, we need to look into this and rephrase I think. Finally, we find that quiescent galaxies have shallower attenuation curves and larger variation than star-forming galaxies.

Keywords: keyword1 – keyword2 – keyword3

* hahn.changhoon@gmail.com

1. INTRODUCTION

Dust in the interstellar medium of a galaxy can dramatically impact the observed light from the galaxy over the full range of the electromagnetic spectrum. Dust emits in the infrared (IR) and modifies the galaxy's stellar radiation through absorption and scatter from the near-infrared (NIR) to ultraviolet (UV). It can, therefore, dramatically impact the physical properties of galaxies we infer from optical and UV light, such as star formation rate (SFR), stellar mass (M_*), or stellar ages (see reviews by Walcher et al. 2011; Conroy 2013). Since these properties are the building blocks for our understanding of galaxies and how they evolve, a better understanding of dust no only provides insights into the physical processes related to dust, but it is also crucial to all galaxy studies.

The combined effect of dust on the spectral energy distribution (SED) of a galaxy is typically described using an attenuation curve, $A(\lambda)$. Observations have now established the major features in $A(\lambda)$. In the UV, the curve steeply rises due to absorptions by small grains. At 2175, in the near-UV (NUV), there is absorption bump referred to as the UV dust bump. Then at longer wavelengths, the curves on take a power-law shape. For an overview, we refer to reviews by Calzetti (2001); Draine (2003); Galliano et al. (2018). Attenuation curves, however, are not universal. Observations find a wide range of attenuation curves in the local Universe (Wild et al. 2011; Battisti et al. 2017; Salim et al. 2018; Salim & Narayanan 2020) as well as at high redshifts (e.g. Reddy et al. 2015; Salmon et al. 2016).

To understand the origin of this variation in attenuation curves, a number of observational works have examined the correlation between dust attenuation and galaxy properties. Using 23,000 star-forming galaxies in the Sloan Digital Sky Survey (SDSS), Wild et al. (2011) found that the slope of the attenuation curves varies strongly with galaxy axial ratio and weakly with specific SFR. Similarly, Battisti et al. (2017), from 5,500 star-forming galaxies, found tentative trends with stellar age, specific star formation rate, stellar mass, and metallicity. Meanwhile, Salim et al. (2018), from 230,000 galaxies in the GALEX-SDSS-WISE Legacy Catalog 2 (GSWLC2), find a significant M_* dependence on the slope. They argue that this is caused by the underlying "attenuation-slope relation", a trend between the amplitude of the V-band attenuation (A_V) and slope where galaxies with higher A_V have shallower slopes. Nevertheless, there is still no clear consensus on the connection between attenuation curves and galaxy properties. Also, studies so far have focused only on star-forming galaxies and little is known about dust attenuation in quiescent galaxies.

Alongside observations, theoretical efforts that model radiative transfer of stellar light through a dusty ISM also provide insights into dust attenuation. Radiative transfer models span a wide range of geometric configurations of stars and dust. For instance, models focused on isolating the physical effects of dust have considered simple slab or shell-like dust geometries illuminated by stellar radiation (e.g. Witt & Gordon 1996, 2000; Seon & Draine 2016). Other models, focused on modeling dust attenuation in galaxies as a whole, have applied 3D dust radiative transfer in hydrodynamic simulations of idealized galaxies (e.g. Jonsson 2006; Rocha et al. 2008; Hayward & Smith 2015; Natale et al. 2015; Hou et al. 2017). Dust attenuation has also been examined in a cosmological context using semi-analytic models (SAMs) that do not track baryonic growth directly

but make simple physically motivated assumptions about the resulting galaxy properties from dark matter growth (*e.g.* Granato et al. 2000; Fontanot et al. 2009; Wilkins et al. 2012; Gonzalez-Perez et al. 2013). Lastly, radiative transfer models have recently been applied to cosmological hydrodynamical simulations (*e.g.* Camps & Baes 2015; Narayanan et al. 2018; Trayford et al. 2020). As in observations, simulations find significant variation in attenuation curves.

Despite their progress, there are still major challenges for radiative transfer models. For instance, they produce attenuation-slope relations that are significantly steeper than observations. Also, many models require significant hand-tuning (*e.g.* propagating rays/photons into particular cells). Assumptions in the underlying dust grain models also produce systematic uncertainties that are difficult to quanitfy (see Steinacker et al. 2013, for a review). Lastly, radiative transfer models are computationally expensive. So applying multiple radiative transfer dust models to multiple simulations for comparisons is prohibitive. Using Markov Chain Monte Carlo sampling with them for parameter exploration or to marginalize over the impact of dust would be *intractable.*

In this paper, we take a different approach and present the Empirical Dust Attenuation (EDA) model, a flexible framework for statistically applying dust attenuation to galaxy populations. The EDA model assigns, to every galaxy, a different dust attenuation curve. The attenuation curves are parameterized with a function-form used in observational studies (Noll et al. 2009) and the parameters of the curve for each galaxy (*e.g.* optical depth, slope) is sampled from distributions set by the EDA model parameters and the galaxy's properties. By sampling the attenuation curve parameters, it produces realistic variations among the attenuation curves. We emphasize that the EDA does not seek to produce realistic dust attenuation for individual galaxies, like radiative transfer models. Instead, it aims to produce realistic dust attenuations for the entire galaxy sample and enable galaxy population-to-population comparisons.

There are a number of advantages to our EDA approach. The EDA uses the same functional-form for the attenuation curves as observational studies, so predictions of the model can easily be compared to observational constraints. We also formulate the EDA parameters so that they are easily interpretable and directly reveal correlations between dust attenuation and galaxy properties. Lastly, the EDA model is computationally inexpensive.

The EDA model, with its flexibility and speed, provides a key crucial in a *forward modeling approach* to comparing simulations to observations (*e.g.* Nelson et al. 2018; Baes et al. 2019; Trčka et al. 2020; **?**).. In the standadrd approach, the galaxy properties (*e.g.* SFR, M_*) predicted by simulations are compared to those derived from observations. Instead, in the forward modeling approach, observables (*e.g.* magnitude, color) are *forward modeled* for each galaxy in the simulations. Then the simulations are compared to observations directly in observational space. With a forward modeling approach, comparisons are not limited by variations, inconsistencies, and biases of different observational methods for measuring galaxy properties (*e.g.* different tracers of SFR or M_*). Selection functions and systematic effects can also be included in the forward model.

Of course to produce realistic observables of simulated galaxies, the forward model must include some prescription for applying dust attenuation. In principle, a radiative transfer model can be used for this purpose; however, its computational cost would severely limit any exploration of the
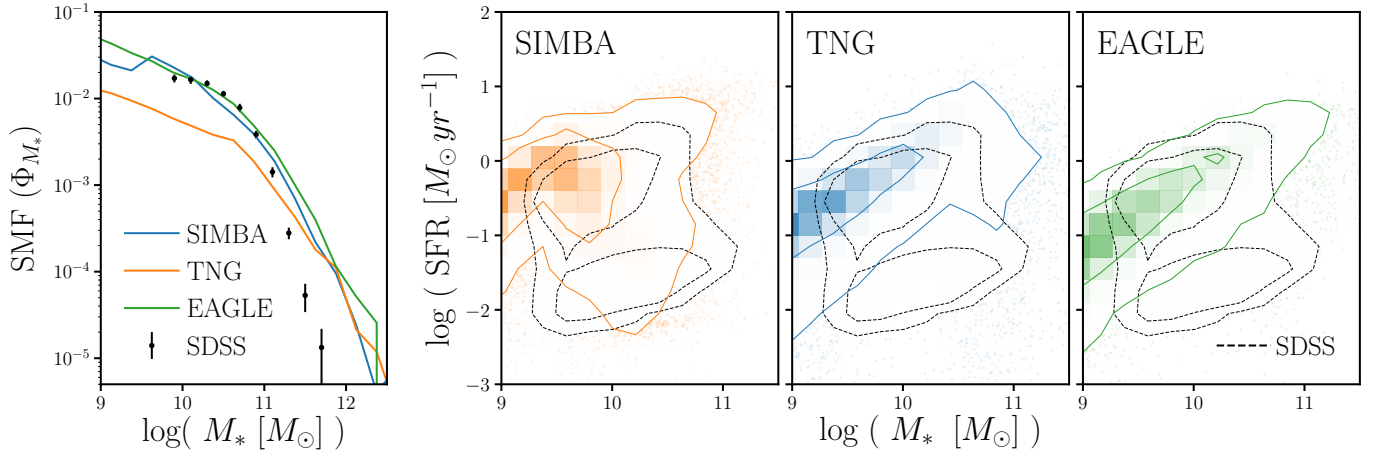
Figure 1. The stellar mass functions, $\Phi(M_*)$ (left-most panel), and M_*-SFR relation (right panels) of galaxies in three cosmological hydrodynamic simulations: SIMBA (orange), TNG (blue), and EAGLE (green). For reference, we include $\Phi(M_*)$ (black) and the $M_* -$ SFR relation (black dashed) of our observational sample from SDSS. Uncertainties for the SDSS $\Phi(M_*)$ are derived using jackknife resampling. We describe the simulations and observations above in Section 2. *Differences in $\Phi(M_*)$ and the $M_* -$ SFR relations among the hydrodynamic simulations highlight how they predict galaxy populations with significantly different the physical properties.*

"dust parameters". With the EDA, however, we can apply a wide range of realistic dust attenuation to simulated galaxies in a matter of seconds. We can, therefore, easily explore and sample the EDA parameter space to infer the relationship between dust attenuation and galaxy properties. *For readers uninterested in dust*, the EDA provides a way to treat dust parameters as *nuisance* parameters and tractably marginalize over them. In other words, the EDA can be used to effectively marginalize over dust attenuation.

In this work, we present a simple EDA model that uses the Noll et al. (2009) attenuation curve parameterization and includes correlations between dust attenuation and galaxy M_* and SFR (Section 3). We apply the EDA to three state-of-the-art cosmological large-scale hydrodynamical simulations, SIMBA, IllustrisTNG, and EAGLE (Section 2), and compare them to observed SDSS galaxies (Section 2.4). In Section 3, we describe our EDA model in detail. Finally, in Section 5, we present the results of our comparison and discuss their implications for our understanding of dust attenuation as well as of its connection to galaxy properties.

2. DATA

In this paper, we present the Empirical Dust Attenuation (EDA) model — a flexible prescription for applying dust attenuation to simulated galaxy populations. We also demonstrate how the EDA can be used in a forward modeling approach to compare galaxy populations in simulations and observations. For our simulations, we use three cosmological hydrodynamical simulations: the Illustris TNG (hereafter TNG), EAGLE, and SIMBA. For our observations, we use a galaxy sample derived from SDSS. Below, we briefly describe the hydrodynamical simulations and the SDSS observations used throughout this work.

In Figure 1, we present the stellar mass functions, $\Phi(M_*)$ left-most panel, and $M_*-\mathrm{SFR}$ relations (right panels) of galaxies in the SIMBA (orange), TNG (blue), and EAGLE (green) cosmological hydrodynamic simulations. We include, for reference, $\Phi(M_*)$ and the $M_* - \mathrm{SFR}$ relation for our observational galaxy sample from SDSS. For the simulations, M_* is the total stellar mass within the host halo, excluding any stellar mass in subhalos; SFR is the instantaneous SFR derived from dense and cold gas. For SDSS, M_* is estimated using `kcorrect` (Blanton & Roweis 2007) assuming a Chabrier (2003) initial mass function and SFR is from the current release of Brinchmann et al. (2004)[1]. The uncertainties for the SDSS SMF are derived from jackknife resampling. Figure 1 illustrates that the hydrodynamical simulations predict significantly different SMFs and $M_* - \mathrm{SFR}$ relations. This difference, which was also recently highlighted in Hahn et al. (2019c), demonstrates that *the hydrodynamical simulations predict galaxy populations with significantly different physical properties*.

2.1. *Illustris TNG*

The Illustris TNG simulation[2] is a cosmological hydrodynamic simulation of comoving volume $(110.7\,\mathrm{Mpc})^3$ (Nelson et al. 2018; Pillepich et al. 2018; Springel et al. 2018). It improves on the original Illustris simulation[3] (Vogelsberger et al. 2014; Genel et al. 2014; public data release by Nelson et al. 2015), by including magneto-hydrodynamics and updated treatments for galactic winds, metal enrichment, and AGN feedback. Most notably, TNG uses a new implementation for feedback from SMBH (Weinberger et al. 2018), where feedback energy is injected in the form of a kinetic AGN-driven wind at low SMBH accretion rates. This new implementation has been shown to alleviate discrepancies found between the original Illustris and observations for $> 10^{13-14}M_\odot$ massive halos.

2.2. *EAGLE*

The Virgo Consortium's EAGLE project[4] (Schaye et al. 2015; Crain et al. 2015; McAlpine et al. 2016) is a publicly available suite of cosmological hydrodynamic simulations constructed using Anarchy (Dalla Vecchia et al. in prep.; see also Appendix A of Schaye et al. 2015), a modified version of the GADGET-3 code (Springel 2005). We use the L0100Ref simulation, which has a comoving volume of $(100\,\mathrm{Mpc})^3$. EAGLE has subgrid models for star formation, stellar mass loss, metal enrichment and stellar feedback that stochastically inject thermal energy in the ISM as in (Dalla Vecchia & Schaye 2012); the feedback energy from AGN is also added to surrounding gas stochastically (Booth & Schaye 2009). Parameters of the stellar feedback and SMBH accretion are calibrated to broadly reproduce the $z = 0$ stellar mass function and galaxy stellar size-stellar mass relation. Meanwhile, the AGN feedback efficiency is calibrated to match the SMBH-galaxy mass relation.

2.3. *SIMBA*

---

[1] http://www.mpa-garching.mpg.de/SDSS/DR7/
[2] https://www.tng-project.org/
[3] http://www.illustris-project.org
[4] http://www.eaglesim.org

The Simba simulation suite (Davé et al. 2019), the successor to Mufasa (Davé et al. 2016, 2017a,b), is a cosmological hydrodynamical simulation constructed using Gizmo, a meshless finite mass hydrodynamics code (Hopkins 2015; Hopkins et al. 2017). Of the simulations, we use 'm100n1024', which has a box size of $(100\,h^{-1}\,\mathrm{Mpc})^3$ and baryonic mass resolution of $1.82 \times 10^7\,M_\odot$. The simulation uses the same subgrid models as Mufasa for H_2 based star formation, decoupled two-phase winds for star formation driven galactic winds, and feedback from Type I supernovae and AGB stars. Meanwhile, it uses updated models for AGN feedback and on-the-fly dust model. Simba uses a two-mode SMBH accretion model, torque-limited accretion for cold gas (Anglés-Alcázar et al. 2017) and Bondi-based accretion for hot gas, and two-mode AGN feedback.

2.4. *SDSS Galaxies*

For our observations, we use a galaxy sample derived from SDSS observations. We start with the $M_* > 10^{9.4}h^{-2}M_\odot$ complete Tinker et al. (2011) volume-limited sample and then impose a $M_r < -20$ completeness cut. The original Tinker et al. (2011) sample is derived from the SDSS DR7 (Abazajian et al. 2009) NYU Value-Added Galaxy Catalog (VAGC; Blanton et al. 2005). In this work, we focus on observables that can be consistently defined and derived in both simulations and observables: M_r, $G-R$, and $FUV-NUV$. For our SDSS sample, we use FUV, NUV, r and g band absolute magnitudes from the NASA-Sloan Atlas[5], which is re-reduction of SDSS DR8 (Aihara et al. 2011) that includes an improved background subtraction (Blanton et al. 2011) and near and far UV photometry from GALEX. These absolute magnitudes are derived using `kcorrect` (Blanton & Roweis 2007), assuming a Chabrier (2003) initial mass function.

2.5. *Forward Modeling Observations*

One of the main goals of this work is to conduct an "apples-to-apples" comparison between the simulations above and observations using a forward modeling approach. A crucial step is to forward model the observables for our simulations — in this work, we use r-band luminosity (M_r), optical color ($G - R$), and UV color ($FUV - NUV$). As the first step, we construct SEDs for all of the simulated galaxies based on their star formation and metallicity histories using the Fleixble Stellar Population Synthesis model (`FSPS`; Conroy et al. 2009, 2010).

For each simulated galaxy, we bin the total stellar mass formed by age (t) and metallicity (Z). We use a consistent t, Z grid for all of the simulations to account for the variable time and mass resolutions. For each point in the t, Z grid, we generate the spectrum of a simple stellar population (SSP) using `FSPS` and take the linear combination of them, weighted by the total stellar mass formed in the bin, to produce the galaxy SED. We use a Chabrier (2003) initial mass function. For further details on how we construct the SEDs, we refer readers to Starkenberg et al. (in prep.).

In the next step of the forward model, we use the EDA model assign dust attenuation curves for each of the simulated galaxies based on their physical properties and apply dust attenuation to their SEDs. We describe the EDAin detail in Section 3.

---

[5] http://nsatlas.org/
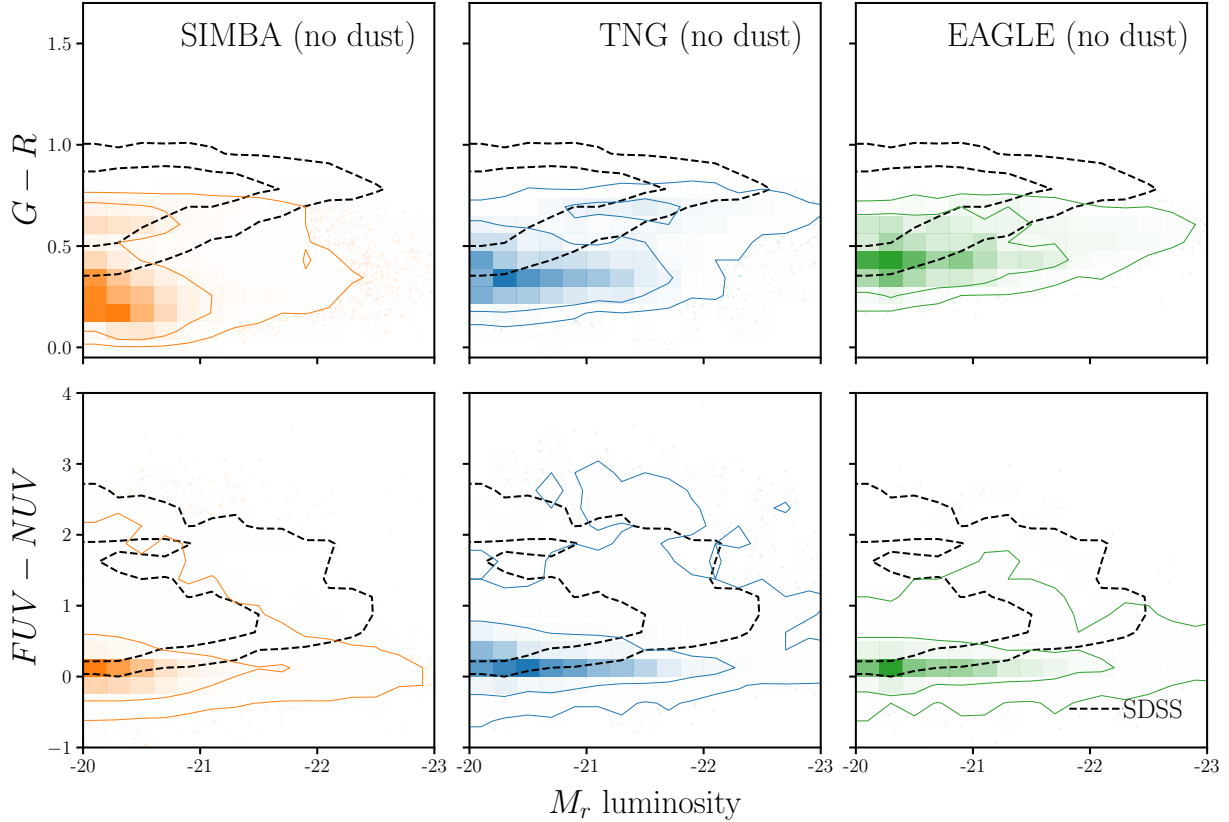
Figure 2. We present the forward modeled optical and UV color-magnitude relations of simulated galaxies in SIMBA (left), TNG (center), and EAGLE (right). The simulations above do *not* yet include the EDAor any prescription for dust attenuation. $(G-R) - M_r$ (top) and $(FUV-NUV) - M_r$ (bottom) are the main observables used throughout the paper. They are derived using SEDs constructed from the star-formation and metallicity of the simulated galaxies. These observables are consistently defined and measured as our SDSS sample (Section 2.5), which we include for comparison (black dashed). *Without dust, the hydrodynamical simulations cannot reproduce the observed optical or UV color-magnitude.*

From the dust attenuated SEDs, we measure the observables by convolving them with transmission curves of the GALEX FUV, GALEX NUV, SDSS g, and SDSS r broadband filters. Lastly, we add realistic noise to M_r, $G-R$, and $FUV-NUV$ We sample the noise from normal distributions, where the standard deviations are drawn from χ^2 fits to the the observed uncertainty distributions from NASA-Sloan Atlas.

In Figure 2 we present the forward modeled optical and UV color-magnitude relations, $(G-R)-M_r$ (top) and $(FUV-NUV) - M_r$ (bottom), for simulated galaxies of SIMBA (left), TNG (center) and EAGLE (right). The observables for the simulations do not yet include any prescription for dust attenuation. Comparison to SDSS observations (black dashed) clearly demonstrate that *without dust attenuation, the hydrodynamical simulations cannot reproduce the observed optical or UV color-magnitude relations.*

3. THE EMPIRICAL DUST ATTENUATION MODEL

In this section we present the Empirical Dust Attenuation (EDA) model, a flexible prescription for applying dust attenuation curves to galaxy populations. With the EDA, we can apply a wide variety of dust attenuation and include correlation between dust attenuation and physical galaxy properties. Later, we demonstrate that we can accurately reproduce SDSS observations with the EDA and use it to test galaxy formation models and shed light on dust in galaxies.

We define the dust attenuation curve, $A(\lambda)$, as

$$F_o(\lambda) = F_i(\lambda)10^{-0.4A(\lambda)} \tag{1}$$

where F_o is the observed flux and F_i is the intrinsic flux. We normalize the attenuation at the V band,

$$A(\lambda) = A_V \frac{k(\lambda)}{k_V} \tag{2}$$

so that A_V determines the amplitude of the attenuation, while $k(\lambda)$ determines the wavelength dependence.

To determine $A(\lambda)$ for each galaxy, we first assign A_V using the slab model from Somerville & Primack (1999); Somerville et al. (2012). In the slab model, A_V is calculated based on the inclination of the galaxy, i, and its optical depth, τ_V:

$$A_V = -2.5 \log \left[\frac{1 - e^{-\tau_V \sec i}}{\tau_V \sec i} \right]. \tag{3}$$

For each galaxy, we uniformly sample i from 0 to $\pi/2$. Then in τ_V we include the correlation between A_V and galaxy properties (M_* and SFR), found in both observations and simulations (*e.g.* Narayanan et al. 2018; Salim & Narayanan 2020). We parameterize τ_V with a simple and flexible linear M_* and SFR dependence:

$$\tau_V(M_*, \mathrm{SFR}) = m_{\tau,M_*} \log \left(\frac{M_*}{10^{10}M_\odot} \right) + m_{\tau,\mathrm{SSFR}} \log \left(\frac{\mathrm{SSFR}}{10^{-10}yr^{-1}} \right) + c_\tau. \tag{4}$$

m_{τ,M_*} quantifies the M_* dependence, $m_{\tau,\mathrm{SSFR}}$ quantifies the SSFR dependence, and c_τ quantifies the overall amplitude. Since τ_V is optical depth, we impose a $\tau_V \geq 0$ limit. The slab model is a naive approximation. In reality, A_V for a galaxy depends on complexities of its star-to-dust geometry, variations in the extinction curves, and other properties beyond just inclination and τ_V. The purpose of the EDA, however, is not to accurately model dust attenuation for individual galaxies, but rather to accurately model the distribution of dust attenuation for galaxy populations. In this regard, the slab model qualitatively reproduces the correlation between A_V and i found in the literature: edge-on galaxies have higher A_V than face-on galaxies (*e.g.* Conroy et al. 2010; Wild et al. 2011; Battisti et al. 2017; Salim & Narayanan 2020). More importantly, the A_V distribution, $p(A_V)$, produced using the slab model with uniformly sampled inclinations closely matches the $p(A_V)$ of our SDSS sample (Figure 8). Replacing the slab model with a more flexible prescription for sampling A_V does not significant impact our analysis (Appendix B). Therefore, we conclude that the slab model is a sufficient, flexible empirical prescription for sampling A_V.

For the wavelength dependence of the attenuation curve, $k(\lambda)$, we use the Noll et al. (2009) parameterization:

$$k(\lambda) = (k_{\mathrm{Cal}}(\lambda) + D(\lambda)) \left(\frac{\lambda}{\lambda_V}\right)^{\delta}. \tag{5}$$

Here $k_{\mathrm{Cal}}(\lambda)$ is the Calzetti (2001) curve:

$$k_{\mathrm{Cal}}(\lambda) = \begin{cases} 2.659(-1.857 + 1.040/\lambda) + R_V, & 6300 \leq \lambda \leq 22000 \\ 2.659(-2.156 + 1.509/\lambda - 0.198/\lambda^2 + 0.011/\lambda^3) + R_V & 1200 \leq \lambda \leq 6300 \end{cases}$$

where $\lambda_V = 5500$ is the V band wavelength. δ is the slope offset of the attenuation curve from k_{Cal}. Since δ correlates with galaxy properties (*e.g.* Leja et al. 2017; Salim et al. 2018), we parameterize δ with a similar M_* and SSFR dependence as τ_V:

$$\delta(M_*, \mathrm{SFR}) = m_{\delta,M_*} \log\left(\frac{M_*}{10^{10}M_\odot}\right) + m_{\delta,\mathrm{SFR}} \log\left(\frac{\mathrm{SSFR}}{10^{-10}yr^{-1}}\right) + c_\delta. \tag{6}$$

$D(\lambda)$ in Eq. 5 is the UV dust bump, which we parameter using the standard Lorentzian-like Drude profile:

$$D(\lambda) = \frac{E_b(\lambda\,\Delta\lambda)^2}{(\lambda^2 - \lambda_0^2)^2 + (\lambda\,\Delta\lambda)^2} \tag{7}$$

where λ_0, $\Delta\lambda$, and E_b are the central wavelength, FWHM, and strength of the bump, respectively. We assume fixed $\lambda_0 = 2175$ and $\Delta\lambda = 350$. Kriek & Conroy (2013) and Tress et al. (2018) find that E_b correlates with the δ for star-forming galaxies $z \sim 2$. Narayanan et al. (2018) confirmed this dependence in simulations. In our EDA model, we assume a fixed relation between E_B and δ from Kriek & Conroy (2013): $E_b = -1.9\,\delta + 0.85$. Allowing the slope and amplitude of the E_B and δ relation to vary does *not* impact our results. In Table 1, we list and describe all of the free parameters in the EDA.

SSFR of galaxies are used to calculate τ_V and δ in Eqs. 4 and 6. However, due to mass and temporal resolutions, some galaxies in the simulations have $\mathrm{SFR} = 0$ — *i.e.* an unmeasurably low SFR (Hahn et al. 2019c). $\mathrm{SFR} = 0$ galaxies account for 17, 19, 10% of galaxies in SIMBA, TNG, and EAGLE, respectively. Since Eqs. 4 and 6 depend on $\log\mathrm{SSFR}$, they cannot be used to derive τ_V and δ for these galaxies. Since $\mathrm{SFR} = 0$ galaxies do not account for a large fraction of our simulated galaxies, we directly sample their observables (G, R, NUV, and FUV) from the distribution of observables for SDSS quiescent galaxies. This way, we ensure that the attenuation of $\mathrm{SFR} = 0$ galaxies does not impact the rest of the EDA parameters. In Appendix A, we discuss the resolution effects in more detail and demonstrate that our results are *not* impacted by other prescriptions for attenuating $\mathrm{SFR} = 0$ galaxies.

In practice, to apply the EDA to a simulated galaxy population, we begin by assigning a uniformly sample inclination, i, to each galaxy. Then based on the EDA parameters, τ_V, and δ are calculated for the galaxy using its i, M_*, and SFR. From τ_V and δ, we determine A_V and $k(\lambda)$, which together gives $A(\lambda)$. Afterwards, we attenuate the galaxy SEDs using Eq. 1 and use the attenuated SEDs to calculate the observables: G, R, NUV, and FUV absolute magnitudes. In
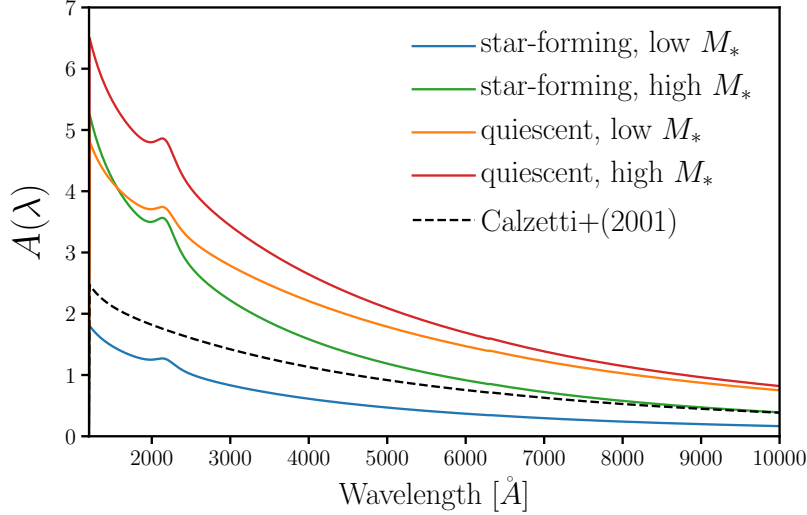
Figure 3. Attenuation curves, $A(\lambda)$, generated by the Empircial Dust Attenuation (EDA) model for galaxies with different SFR and M_*. We include $A(\lambda)$ for star-forming (SFR $= 10^{0.5} M_\odot/yr$) low mass galaxy ($10^{10} M_\odot$; blue), high mass galaxy ($10^{11} M_\odot$; green) and quiescent (SFR $= 10^{-2} M_\odot/yr$) low mass galaxy ($10^{10} M_\odot$; orange), high mass galaxy ($10^{11} M_\odot$; red). All galaxies are edge-on (*i.e.* $i = 0$) and we use EDA parameter values near the center of our prior range (Table 1):$\{m_{\tau,M_*}, m_{\tau,\mathrm{SSFR}}, c_\tau, m_{\delta,M_*}, m_{\delta,\mathrm{SFR}}, c_\delta\} = \{2., -2., 2., -0.1, -0.1, -0.2\}$. For comparison, we include the Calzetti (2001) attenuation curve. In the EDA, the amplitude and slope of $A(\lambda)$ depend on M_*, and SSFR (Eqs. 4 and 6). *The EDA provides a flexible model for applying dust attenuation to galaxies based on their physical properties.*

Figure 3, we present attenuation curves, $A(\lambda)$, generated by the EDA for galaxies with different SFR and M_*: star-forming (SFR $= 10^{0.5} M_\odot/yr$) with low mass ($10^{10} M_\odot$; blue), with high mass ($10^{11} M_\odot$; green) and quiescent (SFR $= 10^{-2} M_\odot/yr$) with low mass ($10^{10} M_\odot$; orange), with high mass ($10^{11} M_\odot$; red). All galaxies are edge-on (*i.e.* $i = 0$) and we use EDA parameters: $\{m_{\tau,M_*}, m_{\tau,\mathrm{SSFR}}, c_\tau, m_{\delta,M_*}, m_{\delta,\mathrm{SFR}}, c_\delta\} = \{2., -2., 2., -0.1, -0.1, -0.2\}$, arbitrarily chosen within the prior range listed in Table 1. For comparison, we include the Calzetti (2001) attenuation curve. The EDA model provides a flexible prescription for applying dust attenuation with a wide range of amplitude and slope to galaxies based on their physical properties.

4. SIMULATION-BASED INFERENCE: APPROXIMATE BAYESIAN COMPUTATION

The DEM provides a flexible model to apply dust attenuation to central galaxies from the hydrodynamic simulations (Section 2) and derive observables which can be directly compared to SDSS observations. For the comparison and the inference of DEM parameters, we use Approximate Bayesian Computation (hereafter ABC; Diggle & Gratton 1984; Tavare et al. 1997; Pritchard et al. 1999; Beaumont et al. 2009; Del Moral et al. 2012). ABC is a simulation-based (or "likelihood-free") parameter inference framework that approximates the posterior probability distribution, $p(\theta \,|\, \mathrm{data})$, without requiring evaluations of the likelihood. Instead, ABC only requires a forward model of the observed data, a prior that can be sampled, and a distance metric that quantifies the "closeness" to the observed data. Since ABC does not require evaluating the likelihood, it does not assume

Table 1. Parameters of the Dust Empirical Model

Parameter	Definition	prior
m_{τ,M_*}	Slope of the optical depth, τ_V, $\log M_*$ dependence	flat $[-5., 5.]$
$m_{\tau,\mathrm{SSFR}}$	Slope of the optical depth, τ_V, $\log \mathrm{SFR}$ dependence	flat $[-5., 5.]$
c_τ	amplitude of the optical depth, τ_V	flat $[0., 6.]$
m_{δ,M_*}	Slope of the attenuation curve slope offset, δ, $\log M_*$ dependence	flat $[-4., 4.]$
$m_{\delta,\mathrm{SFR}}$	Slope of the attenuation curve slope offset, δ, $\log \mathrm{SFR}$ dependence of	flat $[-4., 4.]$
c_δ	amplitude of the attenuation curve slope offset, δ	flat $[-4., 4.]$

any functional form of the likelihood, which can significantly bias the inferred posterior (Hahn et al. 2019b). It also enables us to estimate the posterior using observables with difficult or intractable likelihoods (Hahn et al. 2017a).

In the simplest version of ABC, with a rejection sample framework (Pritchard et al. 1999), a proposal set of parameter values are drawn from the prior. The forward model is run with the proposal parameter values. Then the output of the forward model is then compared to the observed data using the distance metric and a distance threshold. Proposals are drawn until enough of them pass the threshold to sample the posterior. A rejection sampling framework requires a large number of evaluations of the forward model, which can be computationally costly. Many variations of ABC with more efficient sampling strategies have now been applied to astronomy and cosmology (*e.g.* Cameron & Pettitt 2012; Weyant et al. 2013; Ishida et al. 2015; Lin et al. 2016; Alsing et al. 2018). Among these methods, we use ABC in conjuction with Population Monte Carlo (PMC) importance sampling (Hahn et al. 2017a,b, 2019a).

The forward model in our scenario is the hydrodynamic simulation combined with the DEM. Given a set DEM parameters, our forward model produces G, R, NUV, and FUV absolute magnitudes, which can be direclty compared to SDSS observations. We use uninformative uniform priors on each of the DEM parameters and choose ranges to encompass constraints in the literature. The prior ranges of $m_{\tau,M_*}, m_{\tau,\mathrm{SSFR}}, c_\tau$ are chosen to conservatively include the A_V range and M_* and SFR dependence of Narayanan et al. (2018) and Salim & Narayanan (2020). Meanwhile, the prior ranges of $m_{\delta,M_*}, m_{\delta,\mathrm{SFR}}, c_\delta$ are chosen to conservatively include the δ range and M_* and SFR dependence of Leja et al. (2017) and Salim et al. (2018). We list the range of the priors in Table 1. We note that uniform priors on the DEM parameters do not result in uniform priors on τ_V or δ (*e.g.* Handley & Millea 2019). However, we are interested in marginalizing over dust attenuation and understanding the dependence of dust attenuation on galaxy properties, so we use uniformative priors on the DEM parameters and not on the derived τ_V or δ.

ABC also requires a distance metric that quantifies the "closeness" of the forward model output to the observed data. For our distance metric, we use the L2 norm between the summary statistics of the SDSS observation and our forward model:

$$\bar{\rho}(\theta_{\mathrm{DEM}}) = \left[X^{\mathrm{SDSS}} - X^{\mathrm{FM}}(\theta_{\mathrm{DEM}}) \right]^2 . \tag{8}$$

$\theta_{\rm DEM}$ are the DEM parameters. The summary statistics are based on the optical and UV color-magnitude relations, $(G-R)-R$ and $(FUV-NUV)-R$, of central galaxies brighter than $M_r < -20$, where our SDSS central galaxy sample is complete (Figure 2). More specifically, for X, we calculate the number density in 3D bins of $G-R$, $FUV-NUV$, and M_r with widths 0.0625, 0.25, and 0.5 mags. We choose this summary statistic to fully exploit the observable-space predicted by the forward model. Later in Section 5 we discuss other observables that could be included in the analysis.

ABC-PMC begins with an arbitrarily large threshold ϵ_1 and N proposals $\bar{\theta}_1$ sampled from the prior distribution. Each proposal is assigned a weight $w_1^i = 1/N$. Then for subsequent iterations ($i > 1$), the threshold, ϵ_i, is set to the median distance of the previous iteration's proposals. New proposals are drawn from the previous iteration's proposals perturbed by a kernel and kept if their distance is blelow ϵ_i. This is repeated until we assemble a new set of N proposals $\bar{\theta}_i$. The entire process is repeated for the next iteration until convergence is confirmed. For further details on the ABC-PMC implementation, we refer readers to Hahn et al. (2017b) and Hahn et al. (2019a). In Figure 4, we present the posterior distributions of the DEM parameters derived from ABC-PMC for the SIMBA (orange), TNG (blue), and EAGLE (green) hydrodynamical simulations. The contours mark the 68% and 95% confidence intervals.
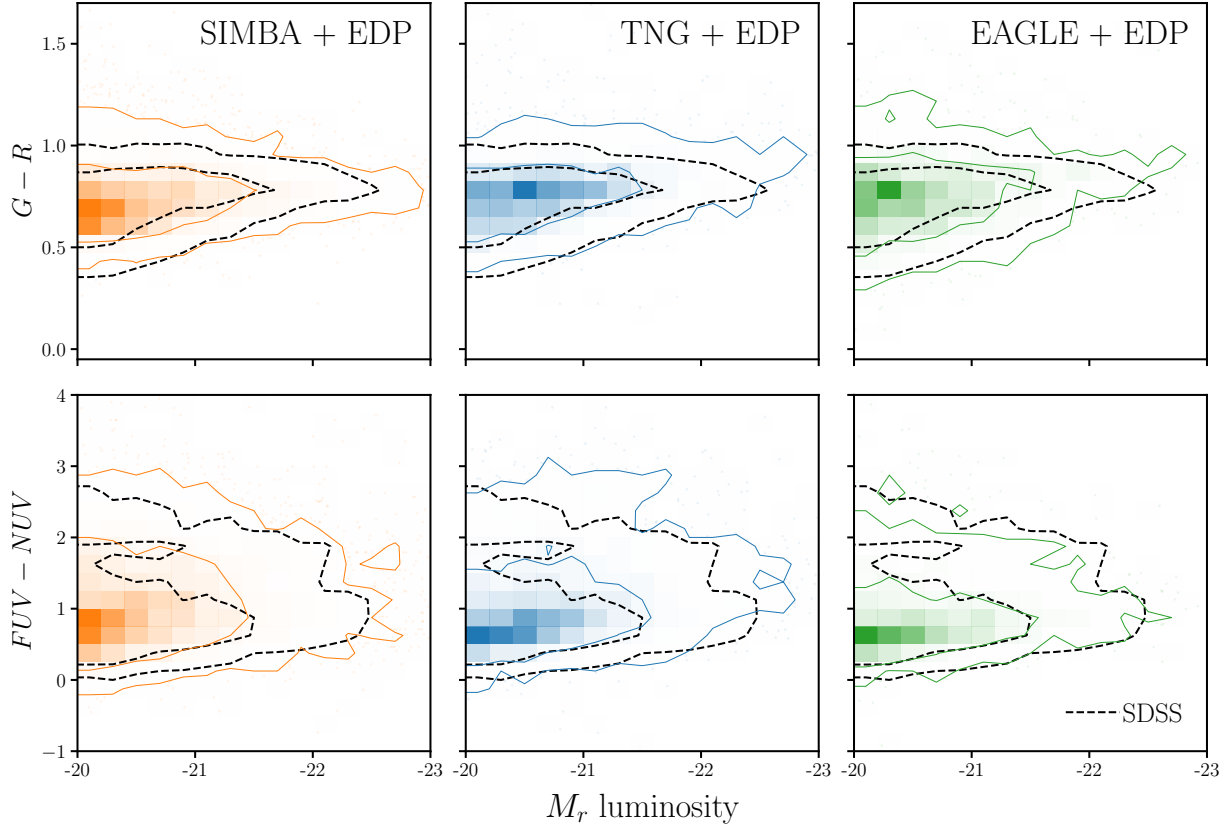
5. RESULTS

5.1. *Reproducing SDSS Color-Magnitude Relations*

In Figure 5, we present the optical and UV color-magnitude relations predicted by the DEM with the median ABC posteriors for the SIMBA (orange), TNG (blue), and EAGLE (green) simulations. We include the SDSS observables for comparison (black dashed). Without any dust attenuation, we previously found that simulations predict dramatically different $(G-R)-M_r$ and $(FUV-NUV)-M_r$ relations than SDSS (Figure 2). In contrast, with the DEM, the optical color-magnitude relations have well-defined red sequences and blue clouds that are consistent with SDSS. The DEM also produces galaxies with $FUV-NUV$ distributions that are consistent with SDSS. We also find good agreement in the galaxy number density at $M_r < -20$: **CH:** numbers

Previous works in the literature have also compared colors and luminosities predicted by simulations to observations. For EAGLE, Trayford et al. (2015) calculate colors and luminosities with the Galaxev population synthesis models and a two-component screen model for dust. More recently, Trayford et al. (2017) calculated optical colors for EAGLE using Skirt, a Monte Carlo radiative transfer code (Camps & Baes 2015), to model the dust. Both Trayford et al. (2015) and Trayford et al. (2017) produce bluer red sequences compared to GAMA observations, at $10^{11.2} < M_* < 10^{11.5}$ for Trayford et al. (2017). Although a detailed comparison is difficult since both works examine all galaxies, not only centrals, the DEM accurately reproduces the position of the SDSS red sequence, even at high M_*. Trayford et al. (2015) also predict significant more luminous blue galaxies than obervations or the DEM. Also using EAGLE and Skirt framework, Baes et al. (2019) find that they overesimtate the observed cosmic SED (CSED) in the UV regime and produce significantly higher $FUV-NUV$ color than GAMA. The DEM, on the other hand, predict $FUV-NUV$ in good agree-
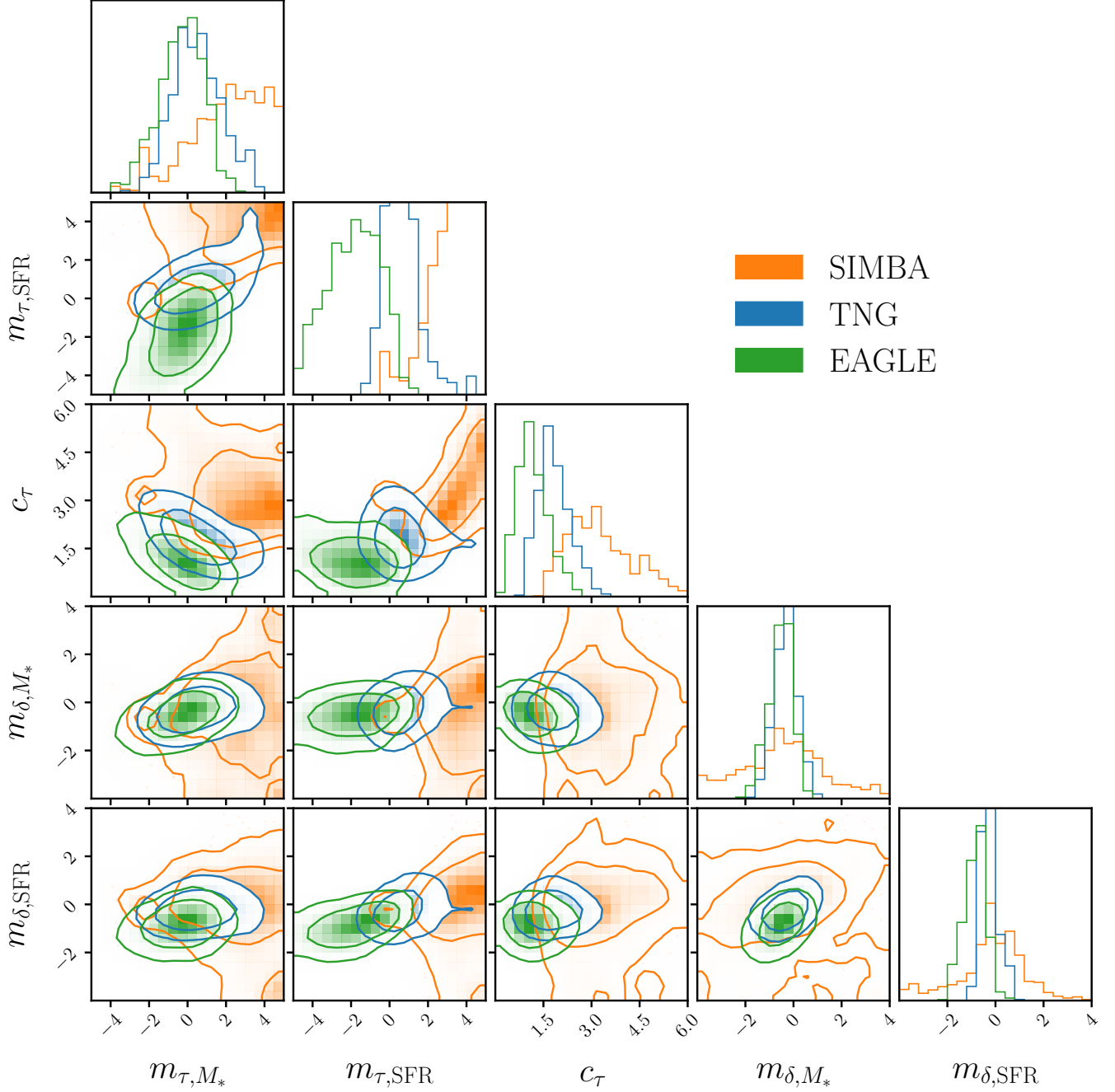
Figure 4. Posterior distributions of DEM parameters for the SIMBA (orange), TNG (blue), and EAGLE (green) hydrodynamical simulations. The contours mark the 68% and 95% confidence intervals. The posteriors are derived using Approximate Bayesian Computation with Population Monte Carlo (Section 4). We focus on the DEM posteriors for TNG and EAGLE since SIMBA requires dust attenuation to reverse the relationship between color and SFR in order to account for it overpredicting low mass starburst galaxies. Based on the posteriors, we find that *galaxies with higher M_* have overall higher dust attenuation and galaxies with lower* SFR *have overall higher dust attenuation.*

Figure 5. The optical and UV color-magnitude relations predicted by the DEM with the median ABC posteriors for the SIMBA (orange), TNG (blue), and EAGLE (green) hydrodynamical simulations. For comparison, we include the $(G-R)-M_r$ (top panels) and $(FUV-NUV)-M_r$ (bottom panels) relations for SDSS (black dashed). With the DEM, the simulations produce dramatically different observables than without any dust prescription (Figure 2). Hence, dust must be account for when interpreting and comparing simulations. Moreover, with the DEMs, all three simulations produce color-magnitude relations consistent with SDSS. Since different simulations can produce reproduce observations by varying dust, dust significantly limits our ability to constrain the physical processes that go into galaxy simulations.

ment with SDSS. For TNG, Nelson et al. (2018) calculate optical colors using a dust model that includes attenuation due to dense gas birth clouds surrounding young stellar populations and also due to simulated distribution of neutral gas and metals. They find bluer red sequence peaks and a narrower blue cloud compared to SDSS. We find neither of these discrepancies with the DEM. *With the DEM, we produce optical and UV color-magnitude relations that are in good agreement with observations, better than previous works, for the SIMBA, TNG, and EAGLE hydrodynamical simulations.*

Figures 5 clearly illustrates that any comparison of simulations must include dust attenuation. Dust dramatically changes the predicted observables of simulations. Without dust (Figure 2), we did not find a clearly bimodality in the optical color-magnitude relation and the simulations predicted UV colors outside of the range of observations. But with attenuation curves assigned from the DEM, simulations successfully reproduce observations. Our results also highlight another key point. Even

for three simulations that produce significantly different SMFs and $M_* - \mathrm{SFR}$ relations (Figure 1), the DEM is able to produce observables that agree with observations. In fact for SIMBA, the DEM reproduces the observations by assigning higher attenuation to star-forming galaxies so that they populate the red sequence while quiescent galaxies populate the blue cloud. This is due to the large number of low mass star-forming SIMBA galaxies that lie well above the SFS (Figure 1), which would otherwise all be luminous blue galaxies not found in observations. Our current understanding of dust, which is encapsulated in the DEM, has enough flexiblity to reproduce observations for simulations that predict galaxy populations with different physical properties, even if it contradicts the established relationship between color and SFR. This means that marginalizing over dust would leave little constraining power on the subgrid galaxy physics of the simulations. Therefore, *current limitations in our understanding of dust in galaxies significant impedes our ability to investigate galaxy formation from simulations.*

5.2. *Reproducing the Observed Attenuation-Slope Relation*

In addition to reproducing the observed color-magnitude relations, we also find good agreement between the attenuation curves of the DEM and observations. In Figure 6, we present the attenuation-slope relation for TNG (blue) and EAGLE (green) with the DEM. The left and right panels present two different measurements of the UV-optical slope $S = A(3000)/A_V$, which is easier to constrain in observations, and δ, the slope offset from the Calzetti (2001) curve that use in the DEM. We include the attenuation and slope for the Milky Way (star) for reference. TNG and EAGLE both predict slopes within $2 < S < 5$ and centered around $S \sim 3.5$. In comparison, for the same $A_V > 0.4$ range as the DEM, observations find slopes within the range $2 < S < 5$ (Calzetti et al. 2000; Burgarella et al. 2005; Johnson et al. 2007; Conroy 2010; Wild et al. 2011; Battisti et al. 2016, 2017; Leja et al. 2017; Salim et al. 2018) in good agreement. We also find that the DEM predicts steeper attenuation curves at lower attenuation. This is consistent with the established attenuation–slope relation. At low attenuation, dust scattering dominates absoprtion so the attenuation curve steepens because red light scatters isotropically while blue light scatters forward (Gordon et al. 1994; Witt & Gordon 2000; Draine 2003). At high attenuation dust absorption is dominant and the attenuation curve is shallower (Chevallard et al. 2013). For the A_V range probed by the DEM, the A_V–slope relation is in good agreement with GSWLC2 galaxies (black shaded Salim & Narayanan 2020). They are also consistent with Leja et al. (2017). We also compare our results to theoretical predictions from radiative transfer models, Inoue (2005) (dotted), the radiative transfer models considered in Chevallard et al. (2013) (dot dashed), and Trayford et al. (2020) (light shaded), which all predict shallower attenuation curves than observations. This is also the case for the Narayanan et al. (2018) attenuation curves (not included). *The attenuation curve slopes from the DEM for are in excellent agreement with observations and better reproduces the observed attenuation–slope relation than radiative transfer models.*

5.3. *The Galaxy − Dust Attenuation Connection*

Next, in Figure 7, we present the normalized attenuation curves of the TNG (blue) and EAGLE (green) DEM for low (top) and high M_* (bottom), star-forming (left) and quiescent galaxies (right).
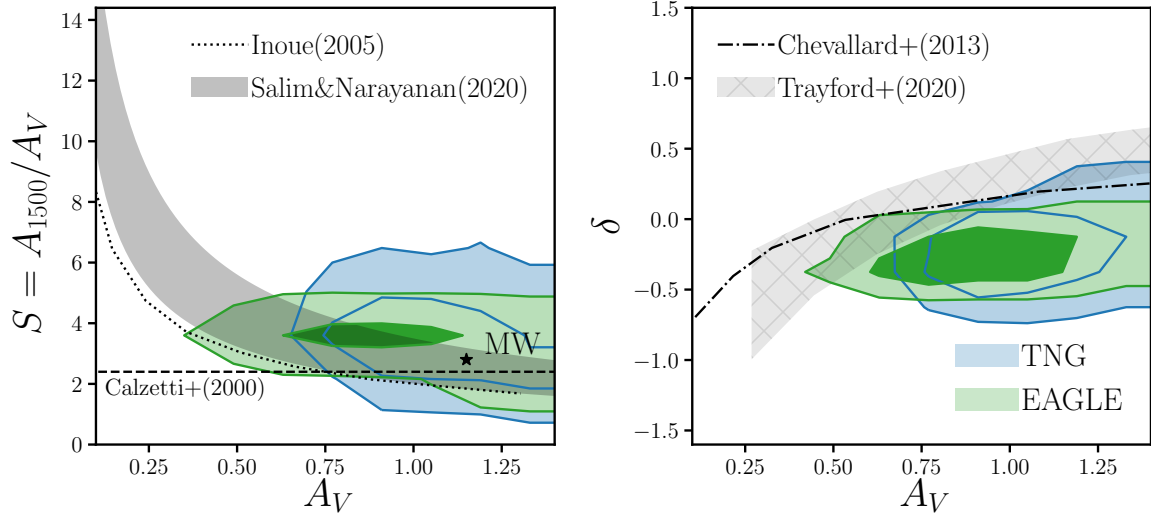
Figure 6. The attenuation-slope relation of the DEM for TNG (blue) and EAGLE (green). We present the relation usng two different measurements of slope, commonly used in the ltierature: $S = A(1500)/A_V$ (left panel) and the slope offset from the Calzetti (2001) curve, δ (right panel). The DEM moodels predict an attenuation-slope relation, where the slope is steeper at lower attenuation, consistent with both observations and radiative transfer models. We only include massive galaxies with $M_r < -20$ so galaxies in our sample have $A_V \gtrsim 0.4$. In this A_V range, the DEM for TNG and EAGLE are in good agreement with observations Salim & Narayanan (2020). In fact, the DEMs match the observed attenuation-slope relation better than radiative transfer model that predict attenuation curves that are too shallow (Inoue 2005; Chevallard et al. 2013; Trayford et al. 2020).
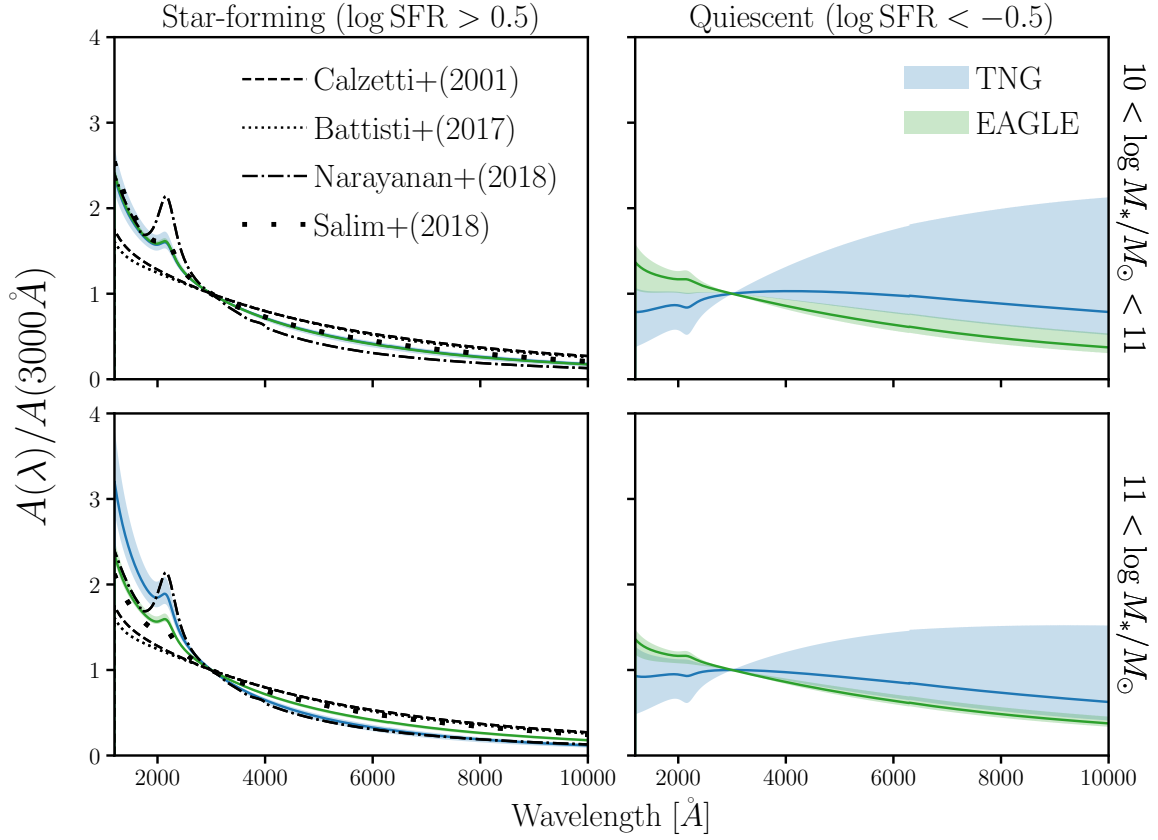
The attenuation curves are normalized at 3000 in order to emphasize their slopes. The DEM includes significant variations in the dust attenuation through the slab model and the dependence on galaxy properties. We present this variation in the shaded region (1σ standard deviation about the median). For comparison, we include $A(\lambda)/A(3000)$ from observations (Calzetti et al. 2000; Battisti et al. 2017; Salim et al. 2018) as well as from simulations (Narayanan et al. 2018). The DEM attenuation curves for star-forming centrals in TNG and EAGLE are in good agreement with the Salim et al. (2018) attenuation curves for $10^{9.5} < M_* < 10^{10.5} M_\odot$ (top left) and $10^{10.5} < M_* M_\odot$ star-forming galaxies (bottom left). They are also consistent with the median curve of Narayanan et al. (2018) star-forming galaxies. On the other hand, they are steeper than the Calzetti et al. (2000) and Battisti et al. (2017) curves. However, we note that the Calzetti et al. (2000) and Battisti et al. (2017) curves are derived from $M_* < 10^{9.9} M_\odot$ star-forming galaxies (below the our M_* range). We find that lower M_* star-forming galaxies have shallower attenuation curves, especially for TNG. If this M_* dependence continues below our M_* range, we expect a better agreement the Calzetti et al. (2000) and Battisti et al. (2017) curves as well. In Salim et al. (2018) and Narayanan et al. (2018), they find large variations in the slopes of the attenuation curve. This is, however, over their entire M_* range. For a narrow M_* range of star-forming galaxies, we find significantly less variation. *Overall, the DEM attenuation curves for star-forming galaxies are in good agreement with attenuation curves in the literature from both observations and simulations.*

So far, we have demonstrated that with the DEM we successfully reproduce the observed color-magnitude relation as well as the attenuation–slope relation. We also find good agreement between the attenuation curves of the DEM and in the literature for star-forming galaxies. Besides reproducing observations and trends in the literature, the constraints on the DEM provide insights into dust attenuation in galaxies. In fact, the parameterization of the DEM makes it especially easy to interpret correlation between dust attenuation and galaxy physical properties. In Figure 4, for all three simulations we find we find significant positive M_* dependence of τ_V ($m_{\tau,M_*} \sim 2$) consistent with previous works in the literature. Burgarella et al. (2005), for instance, found significant positive M_* dependence in FUV attenuation in NUV-selected and FIR-selected samples. Garn & Best (2010) and Battisti et al. (2016) also find positive M_* dependence in SDSS star-forming galaxies. Most recently, Salim et al. (2018) find higher V and FUV attenuation for more masssive star-forming galaxies in GSWLC2. In addition to the M_* dependence, the DEM posteriors also reveal the correlation between dust attenuation and star formation. Ignoring SIMBA, which flips the color versus SFR relation, we find $m_{\tau,\mathrm{SSFR}} \sim -1$ — galaxies with lower SFR have higher attenuation. Observations that examine the relationship between dust attenuation and SFR (*e.g.* Garn & Best 2010; Reddy et al. 2015; Battisti et al. 2016, 2017; Salim et al. 2018) have thus far focused primarily on star-forming galaxies. With the DEM, we confirm that *galaxies with higher M_* have overall higher dust attenuation and find that galaxies with lower* SFR *have overall higher dust attenuation*.

In addition to the correlation with galaxy properties, the DEM also reveals dust attenuation in quiescent galaxies (left panels of Figure 7). This is particularly valuable since there are many challenges to measuring attenuation curves for quiescent galaxies directly from observations. For instance, methods that rely on IR luminosities can be contaminated by MIR emission from AGN heating nearby dust Kirkpatrick et al. (2015). Even SED fitting methods require accounting for AGN MIR emission (Salim et al. 2016; Leja et al. 2018; Salim et al. 2018). SED fitting methods also struggle to tightly constrain dust attenuation due to the degeneracies with star formation history and metallicity (CH: cite?). By forward modeling the optical and UV photometry with the DEM, we do not face these issues. For both TNG and EAGLE, we find that quiescent galaxies have significantly shallower attenuation curve than star-forming galaxies. They also have significantly larger variations than star-forming galaxies.

The DEM produces optical and UV color-magnitude relations overall consistent with SDSS. There are, however, still a few discrepancies between the DEM observables and SDSS. For instance, the DEM produces broader distributions overall than observations. Galaxies in SDSS sharply cut-off above the red sequence, while some galaxies in the DEM broadly extend beyond the cut-off. The DEM also produces galaxies more luminous galaxies than SDSS. Nevertheless, the DEM better reproduces observations than other works. Furthermore, we chose linear parameterization for τ_V and δ in the DEM for simplicity. However, the empirical framework of the DEM can easily be extended to more flexible parameterizations that better reproduce observations — the only challenge would be to find a well-motivated parameterization from observations.

In the DEM, we make a few other assumptions and choices. For simulated galaxies with $\mathrm{SFR} = 0$, we directly sample their observables from the distributions of SDSS quiescent galaxies. These

Figure 7. Attenuation curves of the DEM for TNG (blue) and EAGLE (green) for low (top) and high M_* (bottom), star-forming (left) and quiescent galaxies (right). The attenuation curves are normalized at 3000: $A(\lambda)/A(3000)$. We mark the 1σ standard deviation of the attenuation curves with the shaded region. For comparison, we include measurements of $A(\lambda)/A(3000)$ from observations (Calzetti et al. 2000; Battisti et al. 2017; Salim et al. 2018) as well as from simulations (Narayanan et al. 2018). For star-forming galaxies, the Calzetti et al. (2000) and Battisti et al. (2017) attenuation curves are shallower than the DEM attenuation curves. However, this is primarily driven by the differences in M_* ranges. For Salim et al. (2018), which probe a similar M_* range, we find goood agreement. We also find good agreement with median attenuation curve of star-forming galaxies in Narayanan et al. (2018). With DEM, we can also constrain the attenuation curves of quiescent galaxies, which are challenging to directly constrain from observations. Quiescent galaxies have significantly shallower attenuation curves and larger variations than star-forming galaxies.

SFR = 0 galaxies do not have recent star-formation and also have 0 gas massCHH: @tjitske is this for all sims so we would expect them to also have no dust. However, without attenuating these galaxies, the simulations struggle to reproduce observations. Our prescription for SFR = 0 galaxies ensures that SFR = 0 galaxies do not impact our results, without delving into the issue further. In Appendix A, we describe our prescription in detail and discuss the limitations of the simulations near the mass and temporal resolutions or their gas prescriptions. Another assumption in the DEM is how we assign A_V using the slab model (Eq. 3). The slab model is consistent with the correlation between attenuation and inclination in observations (Conroy 2010; Wild et al. 2011; Battisti et al. 2017; Salim & Narayanan 2020) and simulations (*e.g.* Chevallard et al. 2013; Narayanan et al. 2018;

TODO

Trayford et al. 2020). Furthermore, it is able to reproduce the SDSS A_V distribution (Figure 8). When we further test the robustness of our results by replacing the slab model with a more flexible truncated normal distribution in Appendix B. We find that our results are not significant impacted. We therefore conclude that our results are robust to the assumptions and choices we make in the DEM.

In this work, we present the DEM, a framework for statistically assigning attenuation curves to galaxy populations. We apply the DEM to the SIMBA, TNG, and EAGLE hydrodynamical simulations and forward model optical and UV color-magnitude relations. With the DEM, we reproduce the color-magnitude relations of the SDSS observations for all three simulations. Also, the attenuation curves of the DEM closely reproduce the observed attenuation–slope relation, better than radiative transfer models. Furthermore, the DEM produces attenuation curves that are in good agreement with the literature for star-forming galaxies.

Focusing on the DEM for TNG and EAGLE, we find significant M_* and SFR dependences in the amplitude of dust attentuation, A_V. More massive galaxies have higher dust attenuation; galaxies with lower SFR have higher dust attenuation. The DEM is also able to constrain the attenuation curves for quiescent galaxies, which have few constraints from observations. We find that quiescent galaxies have shallower attenuation curves with larger variation than star-forming galaxies.

By reproducing SDSS observations with the DEM for different hydrodynamical simulations, we demonstrate that accounting for dust attenuation is essential to reproduce observations. However, based on our current understanding of dust there is enough flexiblity to reproduce observations even for simulations that predict galaxy populations with significantly different physical properties. In fact, for SIMBA the inferred dust attenuation reverses the established relationship between color and SFR in order to account for SIMBA overpredicting a large starburst population at $< 10^{10} M_{\odot}$. Since adjusting dust alone can reproduce observations, dust is highly degenerate with the variations in subgrid physics across simulations. In other words, if we were to marginalize over dust we would not be able to differentiate between the various hydrodyanmical models using observations. So detailed comparisons across simulations and to observations likely overinterpret the differences and similarities found in simulations. Therefore, the current limitations in our understanding of dust is a major bottleneck for investigating galaxy formation using simulations.

6. SUMMARY

In this work, we present the DEM, an empirical framework for including dust attenuation in simulated galaxy populations. It uses a parameterization of the attenuation curves motivated from observations (Noll et al. 2009) and a flexible method for sampling the attenuation curve parameters that includes correlations with galaxy properties (M_* and SFR). We apply the DEM to three state-of-the-art hydrodynamical simulations (SIMBA, TNG, and EAGLE) and forward model the optical and UV color-magnitude relations. Afterwards, we compare these forward modeled simulations to observed central galaxies in SDSS using simulation-based inference. Based ont his comparison, we find the following results:

- Dust attenuation is essential for simulations to reproduce observations. With the DEM, we are able to reproduce SDSS observations for all three hydrodynamical simulations. However, SIMBA requires an extreme dust attenuation that reverses the established relationship between color and SFR in order to account for SIMBA overpredicting starburst galaxies at $< 10^{10} M_\odot$.

- The DEM attenuation curves are in good agreement with major observational constraints. They closely reproduce the observed attenuation–slope relation, better than radiative transfer models. We also find significant variation in the attenuation curves as in observations. For star-forming galaxies, the DEM atteunation curves are in good agreement with the literature.

- Focusing on the DEM for TNG and EAGLE, we find significant M_* and SFR dependences in A_V. More massive galaxies have higher dust attenuation; galaxies with lower SFR have higher dust attenuation.

- Lastly, the DEM is able to constrain the attenuation curves of quiescent galaxies, which are poorly constrained by observations. We find that quiescent galaxies have shallower attenuation curves with higher A_V and larger varation than star-forming galaxies.

Our results clearly demonstrate that the DEM can be used to provide insight into dust attenuation. For those uninterested in dust, the DEM also provides a straightforward framework for marginalizing over dust. Although accounting for dust is necessy to reproduce observations, our limited understanding of dust attenatuion allows simulations that predict galaxy populations with significantly different physical properties to reproduce the same observable. Since varying attenuation alone can entirely reproduce observations, dust is highly degenerate with differences in subgrid physics across simulations. After marginalizing over dust, observations do not have the constraining power to differentiate between the various hydrodyanmical models. Hence, detailed comparisons across simulations and to observations likely overinterpret the differences and similarities found in simulations. Therefore, we demonstrate that the current limitations in our understanding of dust is a major bottleneck for investigating galaxy formation using simulations.

Even with the limited statistical power of our M_r complete SDSS central galaxy sample, we derived tight constarints on dust attenuation. Upcoming surveys such as the Bright Galaxy Survey of the Dark Energy Spectroscopic Instrument (DESI; DESI~Collaboration et al. 2016, **CH: Ruiz**et al.2020), the Galaxy Evolution Survey of the Prime Focus Spectrograph (PFS; Takada et al. 2014; Tamura et al. 2016), and the Wide-Area VISTA Extragalactic Survey (WAVES; Driver et al. 2016, 2019) will provide much more statistically powerful observations and at higher redshifts. With these observations, the DEM will be able to more tightly constrain and reveal new insights into dust attenuation.

APPENDIX

A. RESOLUTION EFFECTS

Figure demonstrating imprint SFR=0 leave on the observable space and how we deal with them so we can ignore them...

B. BEYOND THE SLAB DEM

A major assumption of our fiducial DEM is that we sample the amplitude of attenuation from the slab model. The slab model makes the simplifying assumption that dust in galaxies are in a slab-like geometry and illuminated by the stellar radiation source (Somerville & Primack 1999). Then, for a given τ_V, the attenuation depends solely on the orientation of the galaxy. This simplification, ignores any complexities in the star-to-dust geometry that impact the shape of the attenuation curve (Witt Gordon 1996, 2000, Seon Drain 2016).

TODO

Besides its simplifications, the slab model predicts A_V distribution with significant differences than the A_V distributions measured from observations. In Figure 8, we compare the A_V distribution predicted by the slab model (black) to the A_V distribution of star-forming galaxies in our SDSS sample (blue). The A_V values are derived using SED fitting from the Brinchmann et al. (2004) MPA-JHU catalog and how are the SF galaxies classified. The slab model A_V values are derived using Eq. 3 and 4 with M_*s and SFRs from the same SDSS sample and the inclinations, i, are uniformly sampled over the range $[0, \pi/2]$. With $\{m_{\tau,1}, m_{\tau,2}, c_\tau\}$ chosen to reproduce the observed A_V distribution, the slab model can reproduce the overall shape. However, it predicts an extended high A_V tail not found in observations.

TODO

Given these shortcomings of the slab model, we want to ensure that our results do not hinge on the slab model. Modeling the star-to-dust geometries with increased complexities, however, would involve expensive hydrodynamic simulations and dust radiative transfer calculations (*e.g.* Narayanan et al. 2018)jonsson2006, rocha2008, natale2015,hayward smith2015,hou2017,trayford2020. We instead take an empirical approach and implement a flexible model for sampling A_V based on a truncated normal distribution:

TODO

$$A_V \sim \mathcal{N}_T(\mu_{A_V}, \sigma_{A_V}) = \frac{\mathcal{N}(\mu_{A_V}, \sigma_{A_V})}{1 - \Phi\left(-\frac{\mu_{A_V}}{\sigma_{A_V}}\right)}. \tag{B1}$$

Here, $\mathcal{N}$ is the standard normal distribution and $\Phi(x) = \frac{1}{2}\left(1 + \mathrm{erf}(x/\sqrt{2})\right)$ is the cumulative distribution function of $\mathcal{N}$. μ_{A_V} and σ_{A_V} are the mean and variance of the truncated normal distribution. Similar to Eq. 4, we allow μ_{A_V} and σ_{A_V} to depend on the physical properties of galaxies:

$$\mu_{A_V} = m_{\mu,1}(\log\ M_* - 10.) + m_{\mu,2}\log\ \mathrm{SFR} + c_\mu \tag{B2}$$

$$\sigma_{A_V} = m_{\sigma,1}(\log\ M_* - 10.) + m_{\sigma,2}\log\ \mathrm{SFR} + c_\sigma. \tag{B3}$$
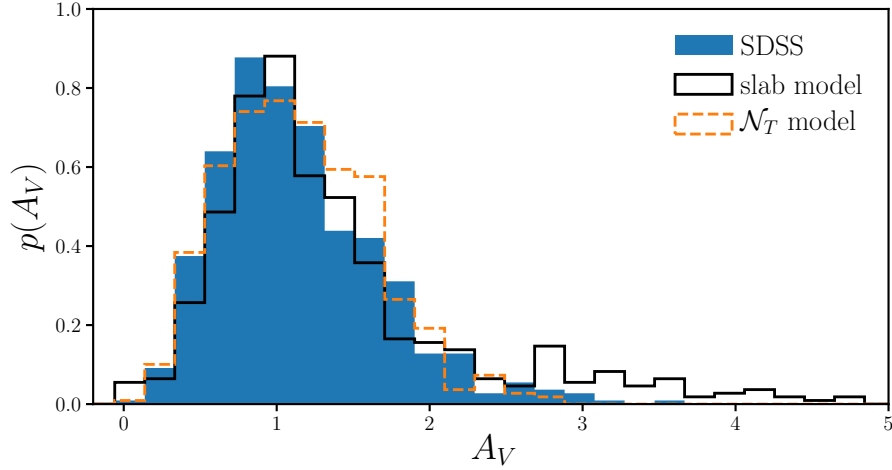
Figure 8. Comparison of A_V distribution of SDSS star-forming galaxies (blue) to predictions from the slab model (Eq. 3; black). detail on how SDSS SF galaxies are classified. The slab model assumes that there's a slab of dust in front of a galaxy. We use $\tau_V = 2$ for the slab model above. Regardless of τ_V, however, the slab model predicts a significantly more asymmetric and peaked A_V distribution than observations. Given this disagreement, *we include in our analysis a DEM with an empirical prescription for A_V based on a truncated normal distribution, which better reproduce the observed A_V distribution* (Section B).

The A_V distribution from our truncated normal (orange dashed) closely reproduces the observed SDSS A_V distribution (Figure 5). N_T is able to reproduce the overall skewness but unlike the slab model, it does not have a long high A_V tail. With more free parameters and a functional form that closely resembles the observed A_V distribution, the truncated normal model provides a flexible altnerative to the slab model and we include it in our analysis.

REFERENCES

Abazajian K. N., et al., 2009, The Astrophysical Journal Supplement Series, 182, 543

Aihara H., et al., 2011, The Astrophysical Journal Supplement Series, 193, 29

Alsing J., Wandelt B., Feeney S., 2018, arXiv:1801.01497 [astro-ph]

Anglés-Alcázar D., Davé R., Faucher-Giguère C.-A., Özel F., Hopkins P. F., 2017, Monthly Notices of the Royal Astronomical Society, 464, 2840

Baes M., Trčka A., Camps P., Nersesian A., Trayford J., Theuns T., Dobbels W., 2019, arXiv:1901.08878 [astro-ph]

Battisti A. J., Calzetti D., Chary R.-R., 2016, The Astrophysical Journal, 818, 13

Battisti A. J., Calzetti D., Chary R.-R., 2017, The Astrophysical Journal, 840, 109

Beaumont M. A., Cornuet J.-M., Marin J.-M., Robert C. P., 2009, Biometrika, 96, 983

Blanton M. R., Roweis S., 2007, The Astronomical Journal, 133, 734

Blanton M. R., et al., 2005, The Astronomical Journal, 129, 2562

Blanton M. R., Kazin E., Muna D., Weaver B. A., Price-Whelan A., 2011, The Astronomical Journal, 142, 31

Booth C. M., Schaye J., 2009, Monthly Notices of the Royal Astronomical Society, 398, 53

Brinchmann J., Charlot S., White S. D. M., Tremonti C., Kauffmann G., Heckman T., Brinkmann J., 2004, Monthly Notices of the Royal Astronomical Society, 351, 1151

Burgarella D., Buat V., Iglesias-Páramo J., 2005, Monthly Notices of the Royal Astronomical Society, 360, 1413

Calzetti D., 2001, New Astronomy Reviews, 45, 601

Calzetti D., Armus L., Bohlin R. C., Kinney A. L., Koornneef J., Storchi-Bergmann T., 2000, The Astrophysical Journal, 533, 682

Cameron E., Pettitt A. N., 2012, Monthly Notices of the Royal Astronomical Society, 425, 44

Camps P., Baes M., 2015, Astronomy and Computing, 9, 20

Chabrier G., 2003, Publications of the Astronomical Society of the Pacific, 115, 763

Chevallard J., Charlot S., Wandelt B., Wild V., 2013, Monthly Notices of the Royal Astronomical Society, 432, 2061

Conroy C., 2010, Monthly Notices of the Royal Astronomical Society, 404, 247

Conroy C., 2013, Annual Review of Astronomy and Astrophysics, 51, 393

Conroy C., Gunn J. E., White M., 2009, The Astrophysical Journal, 699, 486

Conroy C., White M., Gunn J. E., 2010, The Astrophysical Journal, 708, 58

Crain R. A., et al., 2015, Monthly Notices of the Royal Astronomical Society, 450, 1937

DESI~Collaboration et al., 2016, arXiv:1611.00036 [astro-ph]

Dalla Vecchia C., Schaye J., 2012, Monthly Notices of the Royal Astronomical Society, 426, 140

Davé R., Thompson R., Hopkins P. F., 2016, Monthly Notices of the Royal Astronomical Society, 462, 3265

Davé R., Rafieferantsoa M. H., Thompson R. J., 2017a, arXiv:1704.01135 [astro-ph]

Davé R., Rafieferantsoa M. H., Thompson R. J., Hopkins P. F., 2017b, Monthly Notices of the Royal Astronomical Society, 467, 115

Davé R., Anglés-Alcázar D., Narayanan D., Li Q., Rafieferantsoa M. H., Appleby S., 2019, Monthly Notices of the Royal Astronomical Society, 486, 2827

Del Moral P., Doucet A., Jasra A., 2012, Statistics and Computing, 22, 1009

Diggle P. J., Gratton R. J., 1984, Journal of the Royal Statistical Society. Series B (Methodological), 46, 193

Draine B. T., 2003, The Astrophysical Journal, 598, 1017

Driver S. P., Davies L. J., Meyer M., Power C., Robotham A. S. G., Baldry I. K., Liske J., Norberg P., 2016, The Universe of Digital Sky Surveys, 42, 205

Driver S. P., et al., 2019, The Messenger, 175, 46

Fontanot F., Somerville R. S., Silva L., Monaco P., Skibba R., 2009, Monthly Notices of the Royal Astronomical Society, 392, 553

Galliano F., Galametz M., Jones A. P., 2018, Annual Review of Astronomy and Astrophysics, 56, 673

Garn T., Best P. N., 2010, Monthly Notices of the Royal Astronomical Society, 409, 421

Genel S., et al., 2014, Monthly Notices of the Royal Astronomical Society, 445, 175

Gonzalez-Perez V., Lacey C. G., Baugh C. M., Frenk C. S., Wilkins S. M., 2013, Monthly Notices of the Royal Astronomical Society, 429, 1609

Gordon K. D., Witt A. N., Carruthers G. R., Christensen S. A., Dohne B. C., 1994, The Astrophysical Journal, 432, 641

Granato G. L., Lacey C. G., Silva L., Bressan A., Baugh C. M., Cole S., Frenk C. S., 2000, The Astrophysical Journal, 542, 710

Hahn C., Vakili M., Walsh K., Hearin A. P., Hogg D. W., Campbell D., 2017a, Monthly Notices of the Royal Astronomical Society, 469, 2791

Hahn C., Tinker J. L., Wetzel A. R., 2017b, The Astrophysical Journal, 841, 6

Hahn C., Tinker J. L., Wetzel A., 2019a, arXiv:1910.01644 [astro-ph]

Hahn C., Beutler F., Sinha M., Berlind A., Ho S., Hogg D. W., 2019b, Monthly Notices of the Royal Astronomical Society, 485, 2956

Hahn C., et al., 2019c, The Astrophysical Journal, 872, 160

Handley W., Millea M., 2019, Entropy, 21, 272

Hayward C. C., Smith D. J. B., 2015, Monthly Notices of the Royal Astronomical Society, 446, 1512

Hopkins P. F., 2015, Monthly Notices of the Royal Astronomical Society, 450, 53

Hopkins P. F., et al., 2017, arXiv:1707.07010 [astro-ph]

Hou K.-C., Hirashita H., Nagamine K., Aoyama S., Shimizu I., 2017, Monthly Notices of the Royal Astronomical Society, 469, 870

Inoue A. K., 2005, Monthly Notices of the Royal Astronomical Society, 359, 171

Ishida E. E. O., et al., 2015, Astronomy and Computing, 13, 1

Johnson B. D., et al., 2007, The Astrophysical Journal Supplement Series, 173, 392

Jonsson P., 2006, Monthly Notices of the Royal Astronomical Society, 372, 2

Kirkpatrick A., Pope A., Sajina A., Roebuck E., Yan L., Armus L., Díaz-Santos T., Stierwalt S., 2015, The Astrophysical Journal, 814, 9

Kriek M., Conroy C., 2013, The Astrophysical Journal Letters, 775, L16

Leja J., Johnson B. D., Conroy C., van Dokkum P. G., Byler N., 2017, The Astrophysical Journal, 837, 170

Leja J., Johnson B. D., Conroy C., van Dokkum P., 2018, The Astrophysical Journal, 854, 62

Lin C.-A., Kilbinger M., Pires S., 2016, Astronomy and Astrophysics, 593, A88

McAlpine S., et al., 2016, Astronomy and Computing, 15, 72

Narayanan D., Conroy C., Davé R., Johnson B. D., Popping G., 2018, The Astrophysical Journal, 869, 70

Natale G., Popescu C. C., Tuffs R. J., Debattista V. P., Fischera J., Grootes M. W., 2015, Monthly Notices of the Royal Astronomical Society, 449, 243

Nelson D., et al., 2015, Astronomy and Computing, 13, 12

Nelson D., et al., 2018, Monthly Notices of the Royal Astronomical Society, 475, 624

Noll S., Burgarella D., Giovannoli E., Buat V., Marcillac D., Muñoz-Mateos J. C., 2009, Astronomy and Astrophysics, 507, 1793

Pillepich A., et al., 2018, Monthly Notices of the Royal Astronomical Society, 473, 4077

Pritchard J. K., Seielstad M. T., Perez-Lezaun A., Feldman M. W., 1999, Molecular Biology and Evolution, 16, 1791

Reddy N. A., et al., 2015, The Astrophysical Journal, 806, 259

Rocha M., Jonsson P., Primack J. R., Cox T. J., 2008, Monthly Notices of the Royal Astronomical Society, 383, 1281

Salim S., Narayanan D., 2020, arXiv:2001.03181 [astro-ph]

Salim S., et al., 2016, The Astrophysical Journal Supplement Series, 227, 2

Salim S., Boquien M., Lee J. C., 2018, The Astrophysical Journal, 859, 11

Salmon B., et al., 2016, The Astrophysical Journal, 827, 20

Schaye J., et al., 2015, Monthly Notices of the Royal Astronomical Society, 446, 521

Seon K.-I., Draine B. T., 2016, The Astrophysical Journal, 833, 201

Somerville R. S., Primack J. R., 1999, Monthly Notices of the Royal Astronomical Society, 310, 1087

Somerville R. S., Gilmore R. C., Primack J. R., Domínguez A., 2012, Monthly Notices of the Royal Astronomical Society, 423, 1992

Springel V., 2005, Monthly Notices of the Royal Astronomical Society, 364, 1105

Springel V., et al., 2018, Monthly Notices of the Royal Astronomical Society, 475, 676

Steinacker J., Baes M., Gordon K. D., 2013, Annual Review of Astronomy and Astrophysics, 51, 63

Takada M., et al., 2014, Publications of the Astronomical Society of Japan, 66, R1

Tamura N., et al., 2016, in Ground-Based and Airborne Instrumentation for Astronomy VI. eprint: arXiv:1608.01075, p. 99081M, doi:10.1117/12.2232103

Tavare S., Balding D. J., Griffiths R. C., Donnelly P., 1997, Genetics, 145, 505

Tinker J., Wetzel A., Conroy C., 2011, preprint, 1107, arXiv:1107.5046

Trayford J. W., et al., 2015, Monthly Notices of the Royal Astronomical Society, 452, 2879

Trayford J. W., et al., 2017, Monthly Notices of the Royal Astronomical Society, 470, 771

Trayford J. W., Lagos C. d. P., Robotham A. S. G., Obreschkow D., 2020, Monthly Notices of the Royal Astronomical Society, 491, 3937

Trčka A., et al., 2020, arXiv:2003.12576 [astro-ph]

Tress M., et al., 2018, Monthly Notices of the Royal Astronomical Society, 475, 2363

Vogelsberger M., et al., 2014, Monthly Notices of the Royal Astronomical Society, 444, 1518

Walcher J., Groves B., Budavári T., Dale D., 2011, Astrophysics and Space Science, 331, 1

Weinberger R., et al., 2018, Monthly Notices of the Royal Astronomical Society, 479, 4056

Weyant A., Schafer C., Wood-Vasey W. M., 2013, The Astrophysical Journal, 764, 116

Wild V., Charlot S., Brinchmann J., Heckman T., Vince O., Pacifici C., Chevallard J., 2011, Monthly Notices of the Royal Astronomical Society, 417, 1760

Wilkins S. M., Gonzalez-Perez V., Lacey C. G., Baugh C. M., 2012, Monthly Notices of the Royal Astronomical Society, 424, 1522

Witt A. N., Gordon K. D., 1996, The Astrophysical Journal, 463, 681

Witt A. N., Gordon K. D., 2000, The Astrophysical Journal, 528, 799